4-28-2022

The humidity sensing characteristics of PANI-titania nanotube-rGO ternary nanocomposite

Mohamed Morsy
mohamed.morsy@bue.edu.eg

Diamond & Related Materials 126 (2022) 109040

Contents lists available at ScienceDirect

Diamond & Related Materials

journal homepage: www.elsevier.com/locate/diamond

The humidity sensing characteristics of PANI-titania nanotube-rGO ternary nanocomposite

Mohamed Morsy [a,b,*], Amir Elzwawy [c], Ahmed I. Abdel-Salam [b], M.M. Mokhtar [a], A.B. El Basaty [d]

[a] Building Physics and Environment Institute, Housing & Building National Research Center (HBRC), 12311 Dokki, Giza, Egypt
[b] Nanotechnology Research Centre (NTRC), The British University in Egypt (BUE), Suez Desert Road, El-Sherouk City, Cairo 11837, Egypt
[c] Ceramics Department, National Research Centre (NRC), 33 El-Bohouth St., Dokki, Cairo 12622, Egypt
[d] Basic Science Department, Faculty of Technology and Education, Helwan University, Cairo 11281, Egypt

ARTICLE INFO

Keywords:
PANI
Sensors
rGO
Humidity
Nanocomposites

ABSTRACT

Humidity sensors are emerging in diverse technological areas in industrial and agricultural applications in diverse technological areas. Thus, the incorporation of desirable materials for acquiring enhanced performance is demanded. In this work, we have synthesized the PANI-TNT-rGO nanocomposite and applied it as a humidity sensor within the wide span of humidity levels. Incorporating PANI onto the structure increases the number of pores promoting the sensing possibilities. The synthesized TNT-rGO and PANI-TNT-rGO were prepared through two consequential processes, including hydrothermal and in situ polymerization methods. The synthesized TNT-rGO and PANI-TNT-rGO were characterized by X-ray diffraction, FTIR, Raman, scanning electron microscope (SEM), and BET surface area. The sensor's morphological, structural, and BET surface area affirm its quality for the humidity sensing areas. The fabricated sensor could propose a decent contribution in the sensing area with a quick response and recovery times. The sensitivity and sensing mechanism have been evaluated for both composites. The sensitivity of the PANI-TNT-rGO sensor was estimated to be 3.28 MΩ/RH%. The experimental evidence confirmed that the PANI-TNT-rGO exhibited a fast response time of 13 s.

1. Introduction

The measurement and control of humidity are emerging demands in different applications. The relative humidity causes a harmful effect if it exceeds a certain value. The humidity sensors are inherently employed in environmental parameter monitoring, especially in human comfort zones, industrial fabrication processes, agricultural sectors, and food storage [1–5]. The evaluation of humidity sensors is usually related to their sensitivity, response and recovery time, stability, reproducibility, low hysteresis, and fabrication cost. Various materials like ceramics, metal oxide semiconductors, polymers, and carbon nano-based materials were explored to function as humidity sensors [6–9]. They have multiple advantages represented in low cost and fast response [10–13]. Despite these advantages, the obstacles of the current humidity sensor are represented in cross-sensitivity, response and recovery times, and reproducibility [14]. Polyaniline (PANI) is an ideal conducting polymer due to its unique characteristics like ease of preparation, thermal stability, remarkable electrical conductivity, and poor sensitivity to different gases [15–18]. PANI was reported as an effective candidate for various applications such as sensors, actuators, corrosion inhibition [19], lithography, supercapacitor [20,21], and optoelectronic devices [22–24]. Despite its applicability in different directions, some limitations hinder its applications in many areas such as inferior mechanical stability, minimal processability, and insolubility in the conventional solvent [15,25]. Hence, the researchers have devoted their efforts to overcome these limitations via incorporating an organic-inorganic hybrid in humidity sensor devices [26]. The fabrication of PANI/rGO composite improves the thermoelectric properties due to the establishment of hydrogen bonding. Sodium titanate nanostructures with the general formula ($Na_2Ti_nO_{2n+1}$, $3 \leq n \leq 6$) have acquired considerable attention due to their desirable physical and chemical properties for employment in the areas of photocatalysis, chemical absorption, hydrogen storage, lithium and sodium batteries [27]. Inherently, the humidity sensors based on metal oxide suffer from some disadvantages represented in relatively large lag, poor response sensing performance, and long response/recovery time. Many solutions have been proposed to overcome these limitations. One effective approach comprises the combination of metal oxides with another organic polymer [28]. PANI is

* Corresponding author at: Building Physics and Environment Institute, Housing & Building National Research Center (HBRC), 12311 Dokki, Giza, Egypt.
E-mail address: Mohamed.Morsy@bue.edu.eg (M. Morsy).

https://doi.org/10.1016/j.diamond.2022.109040
Received 21 February 2022; Received in revised form 4 April 2022; Accepted 10 April 2022
Available online 28 April 2022

a conjugated conducting polymer having favorable prospects such as low cost, effortless synthesis, good electrical conductivity, and photothermal conversion capability [29]. It has been examined as a prospective sensing material due to its well-regulated electrical conductivity, and good sensitivity. The disadvantages of PANI are lack of solubility and mechanical instability. Therefore PANI has been also combined with polymers such as carbonaceous matrix to improve mechanical stability [30]. The combination of metal oxide and PANI promotes the adsorption sites along with improved thermal stability and electrical conductivity [31].

The incorporation of 2D graphene into sodium titanate and PANI resulted in a promising structure for several applications as demonstrated by several researchers [32–35]. Shuaihao Wang et al., [36] proved that $Na_2Ti_3O_7$NT/g-C_3N_4/rGO ternary composite was successfully synthesized by hydrothermal route. This exceptional structure has open porosity that enables the transport of Na^+ and exhibited outstanding electrochemical performance.

The PANI/ Holmium oxide composite has functioned as humidity as well as a pressure sensor as proposed by T. Ali et al., [37]. In their report, they have exemplified the facility of the in-situ chemical oxidative polymerization process to prepare the PANI/HO_2O_3 composite. The composite was applied as a humidity sensor at RT within 20–90% humidity. The acquired results reveal the decent sensitivity, stability, and reproducibility of the composite based on the PANI incorporation, the porous structure of the PANI is affirmed by the morphological studies which reinforce the humidity sensing capabilities.

The hydrothermal synthesis of ZnO/PANI composite then the employment as a humidity sensor is also performed by W. Gu et al., [5]. The 4 times elevation in the impedance as a result of the humidity change (11–92%) was affirmed. The introduction of PANI promotes better growth of the crystal structure which raises the water adsorption ability. Further, it enhances the H^+ conduction which benefits the humidity sensing abilities. Following these findings, we expect the successful role of the PANI in our proposed structure.

The present study aims to explore the humidity sensing behavior of the PANI@TiO_2 NT-rGO. The designed composite was achieved via two consequential processes including hydrothermal and in situ polymerization. The TiO_2 NT-rGO was prepared via the hydrothermal treatment of TiO_2/GO composite in an alkaline solution. Subsequently, the in-situ polymerization route was introduced to synthesize PANI@TiO_2 NT-rGO nanocomposite. The humidity sensing behavior of the structure was evaluated in a wide range of testing frequencies and under different humidity levels. The phase composition, and structure of composites were verified using XRD, SEM, Raman, FTIR, and surface area. The sensor exhibits noteworthy sensitivity and respectable repeatability with fast response and recovery times.

2. Experimental

2.1. Materials

Ammonium persulfate ($(NH_4)_2S_2O_8$) (APS), Aniline ($C_6H_5NH_2$), toluene, hydrochloric acid (HCl), Titanium (IV) Isopropoxide (Acros, 98+ %), Ethyl alcohol (Fisher chemical, 99.5%), Glacial Acetic acid (Fisher chemical, 99.7%), Sodium hydroxide (Fisher chemical, ≥97%). The deionized (DI) Milli-Q water was used during this experiment.

The above-mentioned chemicals have been exploited as it is without any applied treatment or purification.

2.2. Synthesis of TiO_2 nanoparticles

The nanoparticles were synthesized using the sol-gel method which provides decent merits for the synthesized nanoparticles [38–42]. In a typical method, Titanium Isopropoxide (0.05 mol) were added dropwise to 50 ml of ethanol with sustained stirring for 15 min, followed by the addition of 60 ml of deionized water with stirring for 30 min. Acetic acid (5 ml) was added dropwise to the mixture then the mixture was kept for 2 h with stirring at room temperature.

2.3. Synthesis of TNT-rGO

TNT-rGO was synthesized via the hydrothermal method. The as-prepared TiO_2 Nanoparticles (1.2 g) were added to 10 M NaOH, and then add 0.3 g of the as-prepared GO was synthesized based on the modified hummer method [43–46] The mixture was sonicated via probe sonicator for 15 min at 600 W, then loaded to 100 ml Teflon-lined stainless steel autoclave and performs the hydrothermal reaction at 180°C for 24 h to produce TiO_2 NT-rGO. The obtained material was separated using ultra-centrifugation at 8000 rpm then re-dispersed in deionized water, repeat this step several times till reaching pH 7. Finally, TiO_2 NT-rGO suspension was divided into two portions; the first portion was dried at 80°C overnight and denoted as (HD TiO_2 NT-rGO). The second portion was lyophilized for 24 h using a freeze drier and designated as (FD TiO_2 NT-rGO).

2.4. Synthesis of PANI @ TNT-rGO

The in-situ polymerization route was followed to synthesize PANI @ TNT-rGO.

Ideally, 1 ml of aniline was added into the suspension (200 mg) of TNT-rGO in a 40 ml aqueous solution of 1 M HCl. Then, the mixture was sonicated in a water bath for 30 min. In another glass, 2.5 g of APS was added to a 40 ml aqueous solution of 1 M HCl. In the second step, the suspension of TNT-rGO/aniline was kept in the ice bath at ~5 °C and was stirred vigorously. Then, the previously prepared APS solution was added dropwise into this suspension over 3 h. The obtained 'dark green' solution of PANI@ TNT-rGO nanocomposite was left overnight in the refrigerator and then washed with plenty of water to neutralize its pH. The same methodology was functioned to prepare polyaniline, excluding the addition of TNT-rGO (Fig. 1).

2.5. Characterization techniques

The X-ray diffraction (XRD) patterns of all prepared composites were acquired by Malvern Panalytical Empyrean 3 diffractometer to verify the phase composition and crystal structure. Raman spectra were measured using a confocal Raman microscope (Witec Alpha 300 RA, 514 nm excitation). The surface morphologies of the synthesized composites were examined by Field-Emission Scanning Electron Microscopy (FE-SEM), model Quattro S, Thermo Scientific. FT-IR measurements verified the chemical bonding and interactions. The FTIR spectra were recorded in a spectral range of 4000–400 cm^{-1} with a spectral resolution of 4 cm^{-1} using FT-IR spectrometer (Vertex 70, Bruker). The Brunauer-Emmett-Teller (BET) surface area was determined using NOVA touch 4LX by N2 adsorption.

2.6. Sensor fabrication and evaluation

The fluorinated tin oxide (FTO) substrate was functioned as a scaffold for the sensing material's deposition. The FTO substrate was cleaned carefully with acetone, then deionized water multiple times to remove unwanted impurities, and finally dried at 50 °C. The sensing materials were deposited over FTO substrate using a spin coater. Initially, a small quantity of sensing water was mixed with a minimal amount of deionized water and then grounded minutely to form past. The past was spread over FTO substrate via spin coating at 500 rpm for 3 min, then dried at 50 °C. The schematic diagram representing the sensor's fabrication procedures is displayed in Fig. 2.

The fabricated sensor was subjected to controlled humidity levels from 7% up to 97% RH at room temperature (RT). The saturated salt solutions of LiBr, LiCl, K_2CO_3, NaBr, NaCl, KCl, and K_2SO_4 were stored in a closed vessel to generate a standard humidity level of 7%, 11%, 23%,

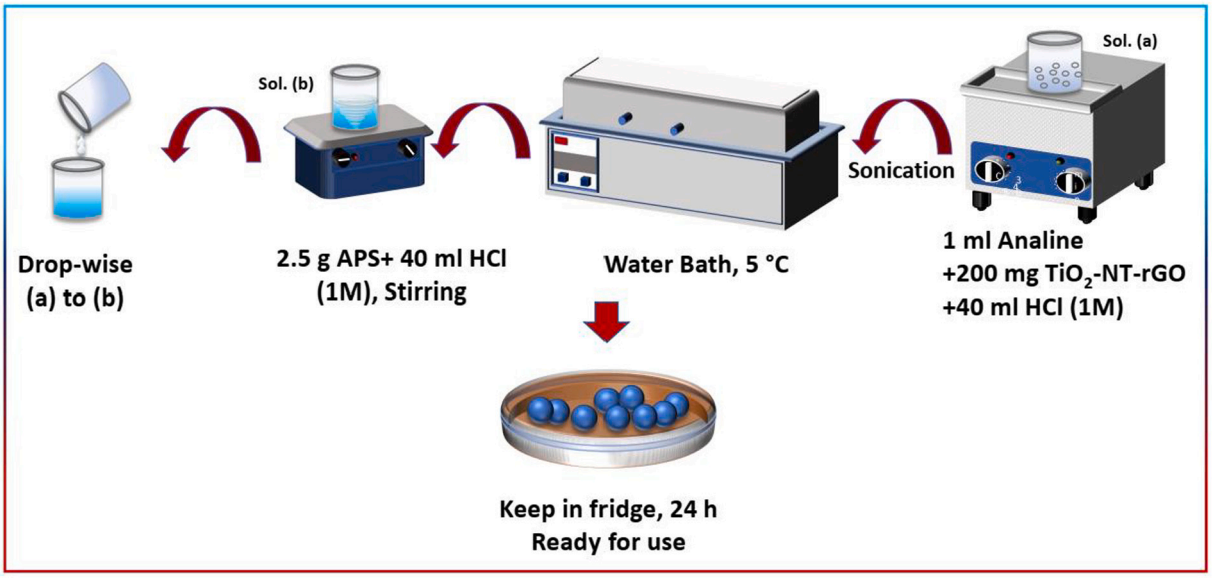

Fig. 1. The schematic illustration for the PANI-TNT-rGO synthesis process.

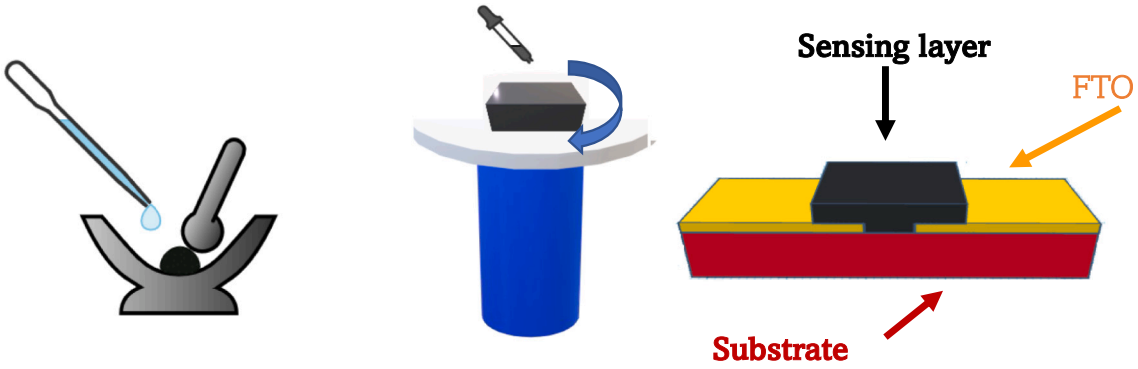

Fig. 2. Schematic illustration of the sensor fabrication process.

43%, 57%, 75%, 84%, and 97% respectively. The sensor was aged for 12 h at a high level and low humidity level. The impedance variation as a function of humidity was measured by applying 1VAC at different testing frequencies. The impedance variation was recorded every 3 s by HIOKI-50 LCR connected to a personal PC. The data were visualized and analyzed in terms of sensitivity, hysteresis, response, and recovery time. The sensitivity was estimated using the following equation [47]:

$$S = \frac{Z_{L-}Z_H}{R_{H-}R_L} \quad (1)$$

where, Z_L is and Z_H represents the impedance value at low and high humidity levels, and R_H, R_L denotes the high and low humidities. The response and recovery times are defined as the time required by the sensor to attain 90% of its maximum variation, respectively, in the case of adsorption and desorption.

3. Results and discussions

In this section, we investigate the structural specifications of the synthesized composite material. The XRD shed light on the structure and main parameters for the obtained composite. The XRD patterns are delivered in Fig. 3.

The XRD pattern of the GO exhibited a diffraction peak at 12, corresponding to (002) planes. Ideally, the polyaniline (PANI) possesses characteristic wide peaks around 15. 03°, 20.50°, and 25.19° which correlates to the diffraction planes of (010), (100), and (110) following the ICSD Card no. 00-065-0826, where the most intense peak occurs at ~20°. This also matches with prior reports [48,49].

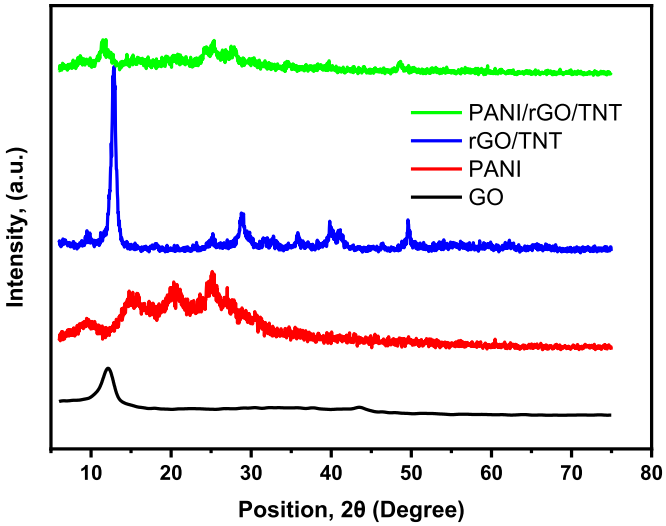

Fig. 3. The XRD patterns of the PANI, rGO/TNT, and PANI/rGO/TNT.

The rGO/TNT exhibits sharper peaks ascribed to the TNT structure, while the rGO peaks are not clear, reflecting the successful coverage of the rGO using TNT.

The apparent planes are noticed at the angles of 9.47°, 12.9°, 28.72°, 35.77°, 39.80°, 40.81°, and 49.63° responding to (100), (0-11), (120), (202), (3-12),(-231), (3-13) planes accordingly. This coincides with the ICSD Card no. 01-084-8818 and the former results either [50]. The incorporation of broad peaked PANI onto the rGO/TNT matrix lessens the intensity of the peaks for TNT and reflects the successful formation of the composite as displayed in Fig. 3. [48]

Fig. 4 displays The FTIR spectrum of the as-prepared TNT-rGO, PANI, and PANI-TNT nanocomposite. The spectra of TNT-rGO show a prominent peak at 1630, 700, 440 cm^{-1} attributed to the stretching vibration of C═C of the rGO [23], Ti—O anatase phase of Titanate nanotubes (TNT), and Ti-O-Ti crystal phonons due to the tubular structure exhibited by TNTs [51], respectively. However, the weak intensity of the C═C, as well as the disappearance of the other peaks of rGO might be due to its lower concentration, and also might be due to growth, covering the PANI for the surface of the TNT which may prevent the appearance of the rGO in the FTIR. The FTIR spectrum of PANI reveals some characteristic peaks at 3227 cm^{-1} is assigned for the N—H stretching mode [52]; stretching vibration modes of C═N and C═C bonds appears at 1570 cm^{-1} and 1490 cm^{-1} respectively for the quinoid and benzenoid rings [53]; the stretching vibration modes that attributed to C—N bond of the benzenoid ring appears at 1294 cm^{-1} and 1238 cm^{-1}. Furthermore, the in-plane bending vibration mode of the C—H bond of N=Q=N, which is characteristic of the protonated PANI appears at 1140 cm^{-1}, which confirms the successful doping of PANI [54]. In addition, the bending vibration mode attributed to aromatic C—H out-of-plane appears at 800 cm^{-1} [52]. The FTIR spectrum of the PANI-TNT-rGO composite contains the characteristic peaks of both TNT-rGO and PANI.

The Raman spectra were carried out to further investigate the chemical bonding of the prepared materials. The Raman spectra of PANI, rGO-TNT, and ternary composite PANI-TNT-rGO are represented in Fig. 5 For PANI, two characteristic bands at 1356 cm^{-1} and 1571 cm^{-1} can be recognized. The band at 1356 cm^{-1} is due to the C–N^{+} stretching, while the band at 1571 cm^{-1} is originated from C═C stretching of the quinoid [55]. The carbon nano-based materials are characterized by two bands named D band and G band. The D band comes from the disorder or structural defect, while the G band corresponds to the first-order scattering of the E_{2g} mode (in-plane vibration of

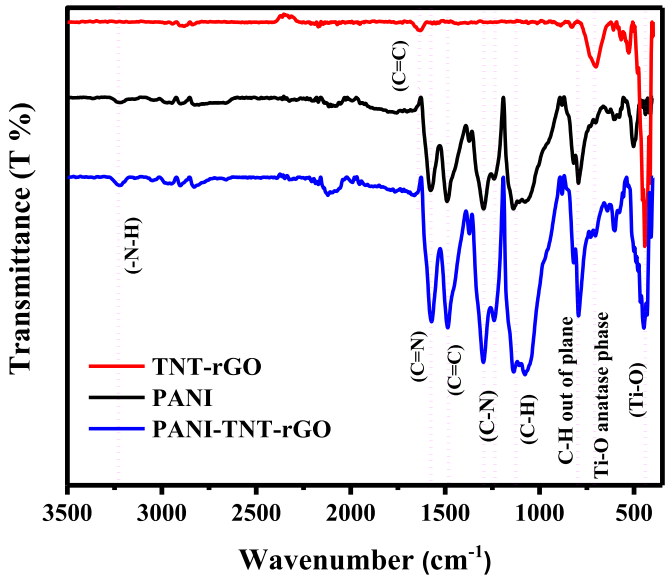

Fig. 4. The FTIR outcomes for the varied synthesized composites.

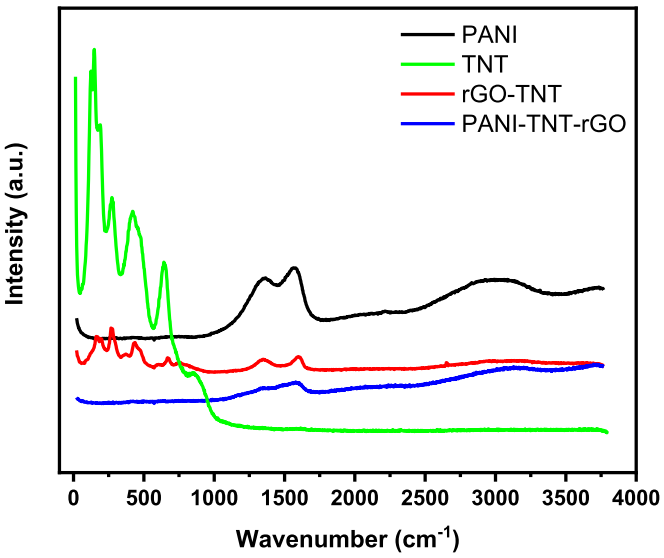

Fig. 5. Raman Spectra for the prepared PANI, PANI-TNT, and PANI-TNT-rGO composites.

sp^2-carbon atoms) [56]. In addition to D band at 1329 cm^{-1} and G band at 1598 cm^{-1}, four bands at 682 cm^{-1}, 440 cm^{-1}, 278 cm^{-1}, and 171 are observed. Characteristically, the metal-containing titanates resulted in a sharp Raman peak; hence the identification of the various phases are presented in the prepared materials is achieved. According to the group theory, the predicted optical phonon mode can be expressed as follows [57]:

$$\Gamma opt = 24Ag + 11Au + 12Bg + 22Bu \quad (2)$$

33 modes are IR active (11Au + 22Bu), and 36 modes are Raman active (24Ag + 12Bg). The bands at 682 cm^{-1}, 278 cm^{-1} arise from Ti—O vibrations in edge-shared and corner-shared TiO_6 octahedra. The band centered around 440 cm^{-1} mainly originate from Na—O—Ti vibrations [58,59]. For the ternary composite PANI-TNT-rGO, the same bands as pare PANI were observed. This is due to the full coverage of both TNT and rGO with PANI. as confirmed by SEM.

The SEM micrographs of the prepared samples are displayed in Fig. 6. Fig. 6a exhibits a granular fibrous structure of PANI. The PANI granules are composed of agglomerated fibers. The TNT-rGO composite of Fig. 6b demonstrates 2D wrinkled graphene sheets and TNT. The TNT has a tubular structure with less agglomeration. The graphene sheets appear as thin multiple layers with crumpled and wrinkled aggregations. The PANI@TiO_2 NT-rGO formed via the interaction between PANI and TNT-rGO. In this structure, the TNT and rGO sheets are coated with PANI fibers as well.

The complete N_2 adsorption-desorption isotherms of all prepared samples are displayed in Fig. 7. According to the International Union of Pure and Applied Chemistry (IUPAC) classification, all isotherms belong to type III. In the case of type III isotherm, the adsorbent-adsorbate interactions are relatively weak, and the adsorbed molecules are assembled all over the active sites on the surface of a material. The BET surface areas of PANI, rGO-TNT, and PANI-TNT-rGO were estimated to be 104.233, 161.544, and 133.047 m^2/g, respectively as represented in Table 1. Notably, the surface area of rGO-TNT is greater than pure PANI. On contrary, the estimated BET surface area of PANI-TNT-rGO is lower than the rGO-TNT composite. This could be due to the rGO sheets that have an elevated surface area that enhances the estimated BET surface area [60], Simultaneously, in the case of PANI-TNT-rGO, the PANI cover the TNT which may decrease the calculated surface area. The SEM images in Fig. 6 demonstrated that PANI fully covers the rGO-TNT. The pore radius and total pore volume follow the above-described trend. The pore radius of all samples indicates the presence of micropores.

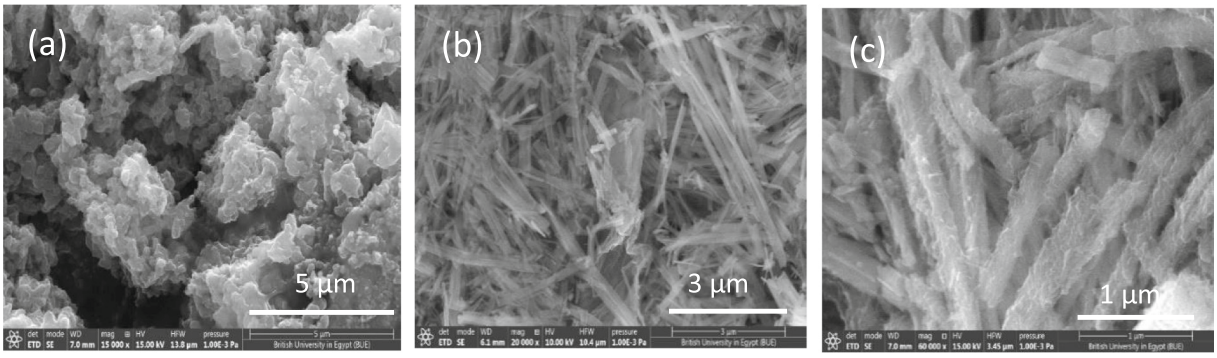

Fig. 6. The scanning electron microscopy (SEM) results for (a) PANI, (b) TNT-rGO, and (c) PANI-TNT-rGO composites.

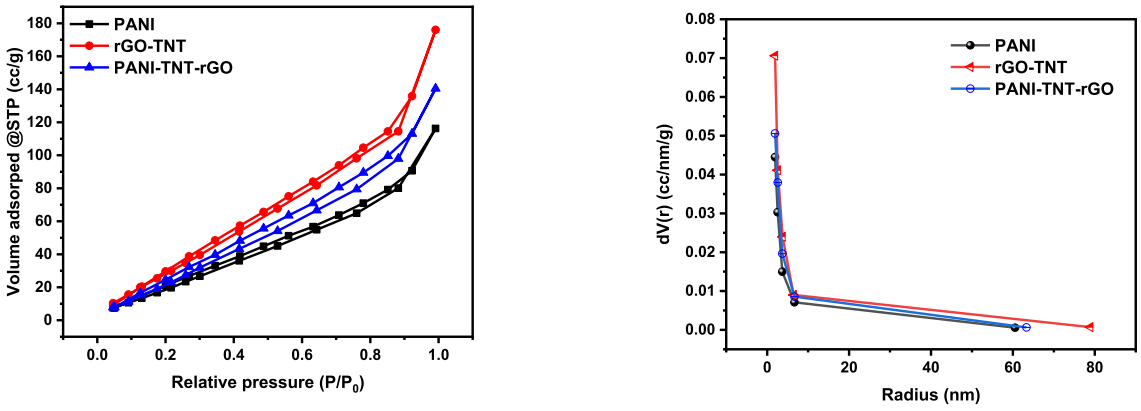

Fig. 7. a) The adsorption response for the synthesized composite structures, and b) the desorption.

Table 1
The BET results for the synthesized composites.

Sample name	Average pore size, nm	BET surface area, m^2/g	BJH surface area, m^2/g	BJH pore volume, cm^3/g	Pore radius, nm	Total pore volume
PANI	3.46	104.233	65.144	0.158	1.920	0.1803
TNT-rGO	3.379	161.544	95.496	0.239	1.931	0.2272
PANI-TNT-rGO	3.2740	133.047	79.9166	0.192013	1.91808	0.21780

3.1. Humidity sensing characteristics

The humidity sensing behavior of the rGO-TNT and PANI-TNT-rGO composites was investigated in a big range of humidity from 7% up to 97% using 1 VAC. The sensor has been tested at different frequencies to elucidate the effect of applied frequency on the response, as illustrated in Fig. 8. Remarkably, the impedance of the PANI-TNT-rGO is lower than rGO-TNT by two orders of magnitude due to the PANI presence.

Inherently, the impedance variation decreases as the frequency increases. This behavior is related to the polarizability of adsorbed water molecules. As the frequency increases the water molecules cannot follow the change in polarity; hence the impedance variation is lower. Accordingly, the prepared sensors will be tested at 100 Hz [10,61]. Fig. 8 demonstrates the variation of impedance as a function of relative humidity for rGO-TNT and PANI-TNT-rGO. It was demonstrated through experimental evidence for both sensors that the impedance increases as the relative humidity increase up to 23%, then decreases with increasing the humidity level. The PANI-TNT-rGO sensor, as compared to the rGO-TNT sensor, suffers from a dramatic decrease in its impedance when the humidity increases above 43%. The sensitivity of the PANI-TNT-rGO sensor was estimated to be 3.28 MΩ/RH%. A more detailed investigation of the PANI-TNT-rGO sensor has been carried out (Fig. 9).

The emeraldine base PANI contains oxidized (—N=) and reduced (_NH_) forms, as represented in Fig. 4. These two forms can be protonated due to the presence of un-bonded electron pair on the nitrogen atom as described by the following equations [62]:

$$NH \rightarrow NH_2^+ \text{ and } N \rightarrow NH^+ \quad (3)$$

The conduction mechanism of the PANI is governed by the electron hopping from protonated reduced form (NH_2^+) to the protonated oxidized form (NH^+). Since (NH_2^+) is incapable of leaving an electron without earlier leaving a proton; thus the electron hopping occurs conditionally before the transformation of a proton. This type of conduction occurs in the presence of water molecules [63].

$$NH_2^+ + H_2O \rightarrow NH + H_3O^+ \quad (4)$$

Thus, in other words, ionic and electronic conduction happens during humidity sensing [64].

The response and recovery times are defined as the time required by the sensor to attain 90% of its original value in the case of adsorption and desorption respectively. Based on this definition the response time and recovery times were calculated to be 13 s and 200 s, respectively, as represented in Fig. 10. The data revealed that the response time is greater than the response time. Famously, the desorption of water molecules requires more energy than adsorption, hence the desorption of water molecules from the sensor's surface takes much more time than the desorption of water molecules (Table 2).

Complex impedance spectroscopy (CIS) is a powerful technique for explaining the sensing mechanism of the humidity sensor [71,72]. The

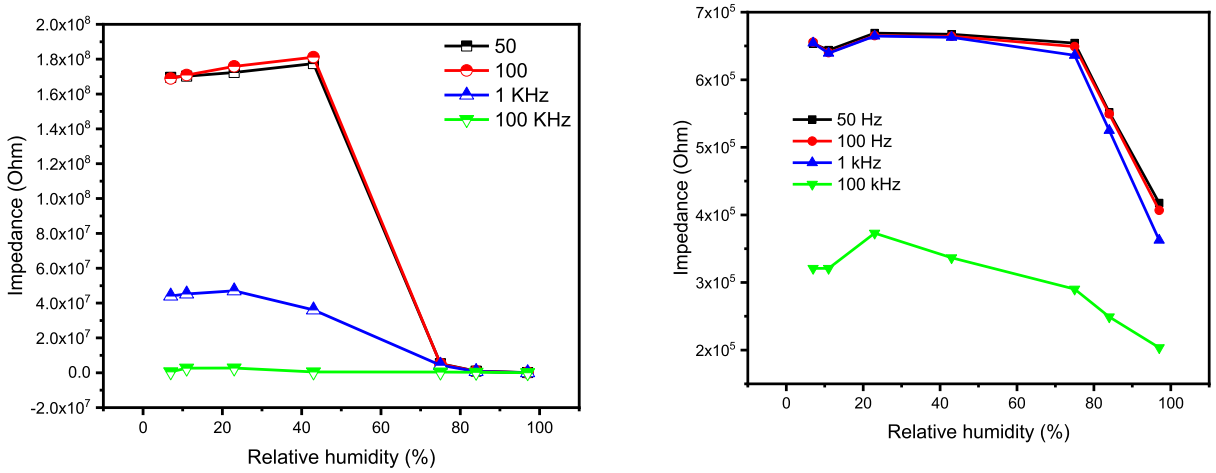

Fig. 8. The resultant alteration of the impedance magnitude as a function of the relative humidity for rGO-TNT (left) and PANI-TNT-rGO (right) at varied frequencies.

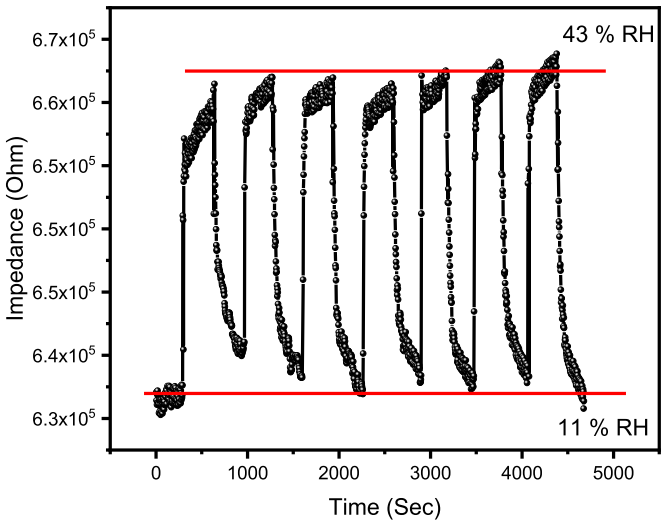

Fig. 9. The stability and repeatability of the sensor times within two dissimilar humidity levels.

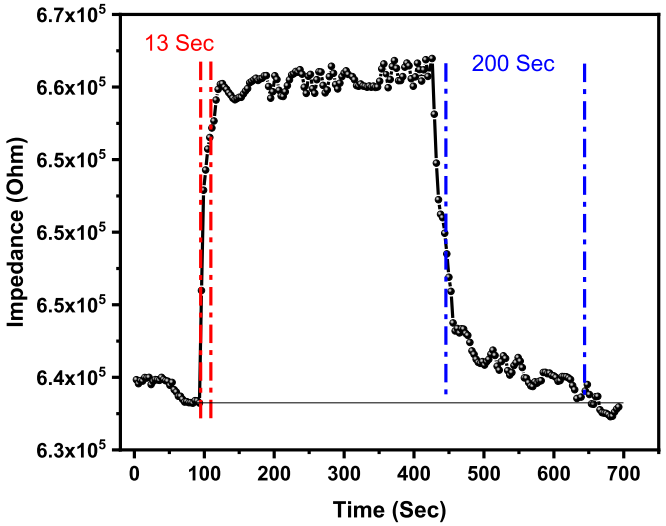

Fig. 10. The illustration of the response and recovery times for the synthesized PANI-TNT-rGO sensor.

CIS spectra for the fabricated sensors at different RH values and different frequencies from 100 Hz to 5 MHz were evaluated. The CIS curves of the rGO-TNT are depicted in Fig. 11. At a low humidity level, the CIS demonstrates a straight line, while a semicircle starts to appear with a further increase in the humidity level. A tail at the low-frequency region appears for humidity levels greater than 43%. At the beginning and under low humidity circumstances, the water molecule is chemically adsorbed via a double hydrogen bond, thereby hindering the movement of charge carriers, so the conductivity is originated from the intrinsic charge carriers. More water molecules are physically adsorbed with the further increment in humidity level, thereby initiating ionic conduction. A short line starts to appear in a lower frequency range at elevated humidity levels. This short line is related to the Warburg impedance (Zw) due to the diffusion process of charge carriers. At this stage of conduction, the water molecules form a continuous layer of water; thereby, the generated protons are transferred to the neighboring water molecules, known as the Grotthuss chain reaction [1].

The CIS curves for the PANI-TNT-rGO are depicted in Fig. 12. Remarkably, the semi-circle is apparent at humidity levels from 7% to 75%. The semicircle indicates that the adsorbed water molecule on the sensor's surface is dissociated to OH^- and H_3O^+ for ionic conduction. The appearance of the semicircle at a low humidity level is due to the presence of PANI as described by Eq. (4). For high humidity levels, a short line is observed at a lower frequency region. The curvature of the semi-circle decreases with increasing the humidity level.

The sensing mechanism of humidity sensors relies on the chemisorption and physisorption of water molecules onto the sensor's surface. At relatively low humidity the water molecules are chemically adsorbed and dissociate on the sensor's surface to form protons (H^+) and hydroxyl groups (OH^-). At this stage the water molecules are adsorbed on the sensor's surface via a double hydrogen bond; thereby the sensor reveals high impedance. With the growing humidity level, more water layers are physically adsorbed, then the water molecules interact with the generated OH^- group to produce hydronium ions. At this stage, the produced hydronium can move freely between adjacent water molecules known as Grotthuss chain reaction.

$$H_2O \rightarrow H^+ + OH^- \quad (5)$$

$$H_2O + H^+ \rightarrow H_3O^+ \quad (6)$$

$$H_3O^+ + H_2O \rightarrow H_3O^+ + H_2O \quad (7)$$

Table 2
The proposed sensor's performance compared to other reported sensors in previous works.

Sensing material	Fabrication method	Measurement range	Sensor response time (s)	Sensor recovery time (s)	Ref.
GO/PANI/TNT	In-situ chemical oxidative polymerization	23–97% RH	13	200	This work
Orange dye-polyaniline composite	Composite films were deposited on glass substrates between pre-deposited silver electrodes	30–90% RH	34	450	[65]
PANI/Pr_2O_3 composite	In situ polymerization	15–95% RH	377	453	[66]
Nanogranular (Ng) PANI-paper	In Situ Synthetization	16–96% RH	1300	2809	[67]
Spandex covered yarns (SCY)-PANI fibers	The as-prepared SCYs were immersed in the polymerization solution of aniline	27–98% RH	400-30	–	[68]
PANI-Nb_2O_5	Chemical polymerization of aniline without/with Nb_2O_5	25–95% RH	80	90	[69]
Poly (lactic acid)/PANI–ZnO composite	Hydrothermal and in situ polymerization followed by electrospinning	20–90% RH	85	120	[70]

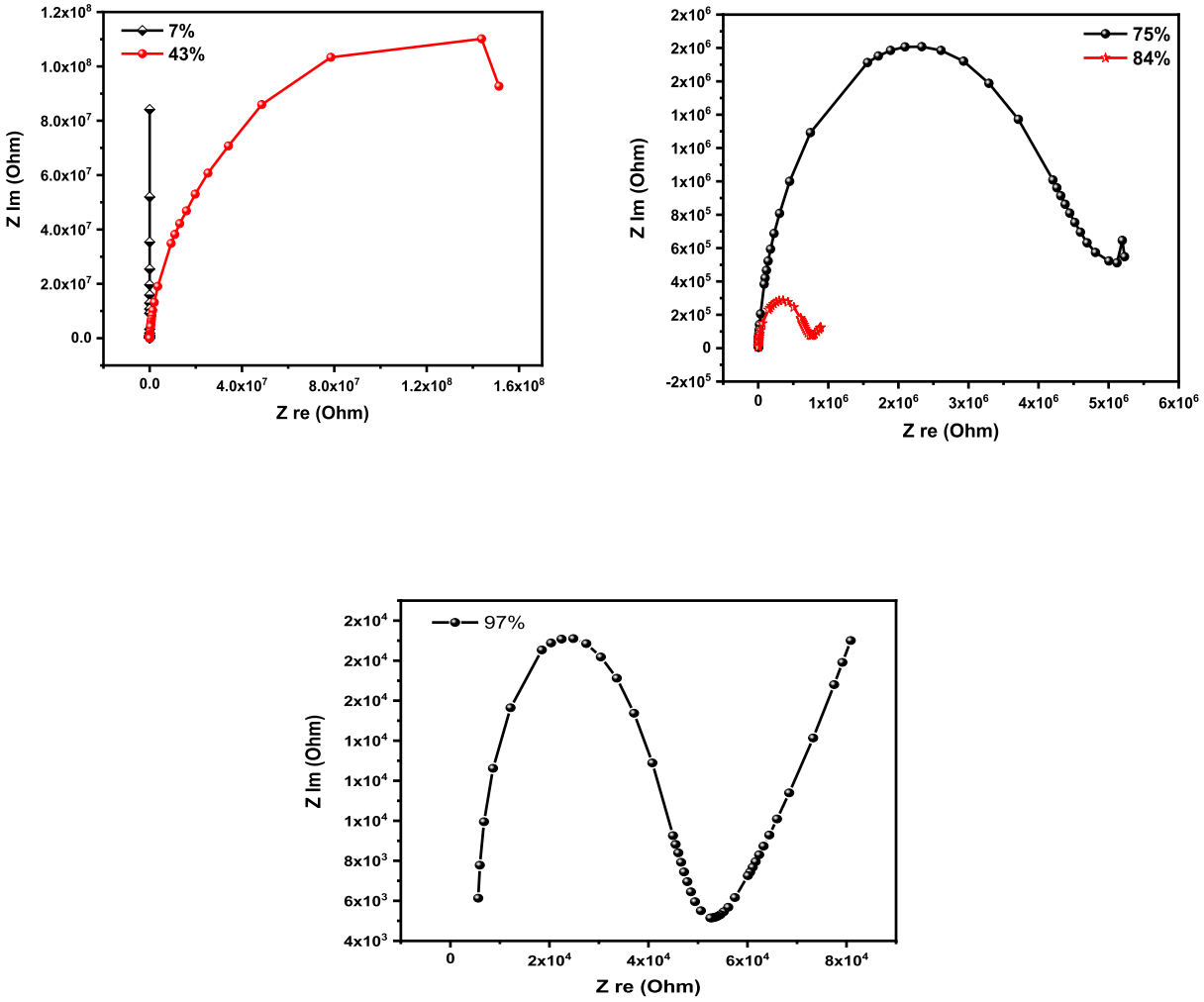

Fig. 11. The propagation of the imaginary part of the impedance with the real part of the impedance for the rGO -TNT sensor at various humidity levels.

The equivalent circuit of semi-circle (7% up to 75%) can be represented by a resistor and capacitor in parallel. For a high humidity environment, the Warburg impedance (ZW) is predominant, and the equivalent circuit can be represented by resistor and capacitor in parallel and then in series with the resistor. The presence of PANI in the structure plays an important role, where the PANI contains a huge number of N—H groups, Which in turn facilitates the transmission of the generated Protons (H^+) and then increases the response and sensitivity. This behavior can be described using the following equations [28]:

$$H^+ + NH \rightarrow NH_2^+ \quad (8)$$

$$NH_2^+ + H_2O \rightarrow NH + H_3O^+ \quad (9)$$

4. Conclusion

This reports successfully synthesized the PANI-TNT-rGO composite via the feasible combination of hydrothermal treatment and polymerization. The morphology of the prepared composite and its derivatives were evaluated. The spectral and the bands of the structures were determined. The XRD, FTIR, and Raman measurements confirm the successful incorporation of PANI, TNT, and rGO in a unified structure.

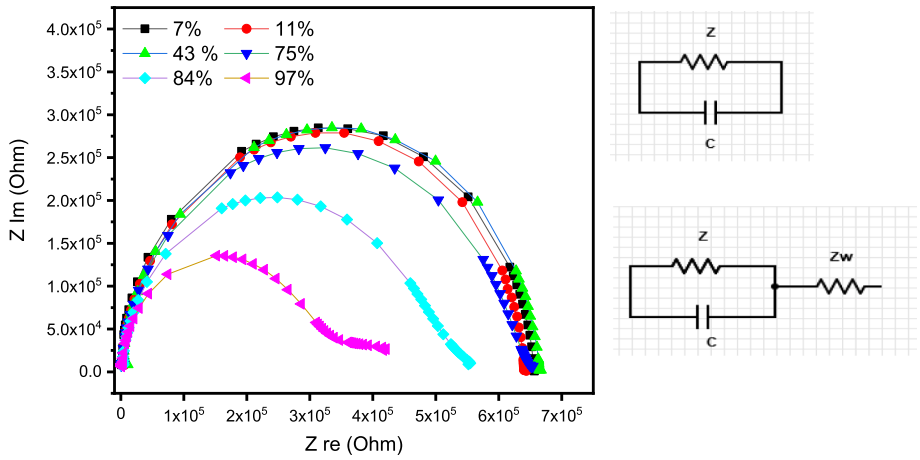

Fig. 12. The combined change of imaginary vs. real parts of impedance at various humidities.

The PANI covered the TNT as indicated by SEM observations. The sensor's performance at varied frequencies and surrounding humidity levels is monitored. The fabricated sensors display a fast response and recovery times referred to as 13 s and 200 s for the former and the latter correspondingly. The sensing mechanism largely depends on the presence of PANI in the prepared structure.

Funding statement

This research received no specific grant from any funding agency in the public, commercial, or not-for-profit sectors.

Ethics statement

Hereby, All authors consciously assure that for the manuscript "The humidity sensing characteristics of PANI/rGO/TNT nanocomposite", the following is fulfilled:

1) This manuscript is the authors' own original work, which has not been previously published elsewhere.
2) The paper is not currently being considered for publication elsewhere.
3) The paper reflects the authors' own research and analysis in a truthful and complete manner.
4) The paper properly credits the meaningful contributions of co-authors and co-researchers.
5) The results are appropriately placed in the context of prior and existing research.
6) All sources used are properly disclosed (correct citation). Literally copying of text must be indicated as such by using quotation marks and giving proper reference.
7) All authors have been personally and actively involved in substantial work leading to the paper, and will take public responsibility for its content.

Declaration of competing interest

The authors declare that there are no conflicts of interest regarding the publication of this paper.

References

[1] H. Moustafa, M. Morsy, M.A. Ateia, F.M. Abdel-haleem, Ultrafast response humidity sensors based on polyvinyl chloride/graphene oxide nanocomposites for intelligent food packaging, Sensors Actuators A Phys. 331 (2021), 112918, https://doi.org/10.1016/j.sna.2021.112918.

[2] S. Kundu, R. Majumder, R. Ghosh, M. Pradhan, Relative humidity sensing properties of doped polyaniline-encased multiwall carbon nanotubes: wearable and flexible human respiration monitoring application, J. Mater. Sci. (2019), https://doi.org/10.1007/s10853-019-04276-z.

[3] N.P. Putri, D.W. Pravitasari, M.S. Kumar, K.Y. Yasoda, Synthesis of polyaniline/cellulose composite as humidity sensor, in: Synthesis of Polyaniline/Cellulose Composite as Humidity Sensor, 2018.

[4] H. Parangusan, J. Bhadra, Z. Ahmad, S. Mallick, F. Touati, N. Al-thani, Talanta capacitive type humidity sensor based on PANI decorated cu – ZnS porous microspheres, Talanta 219 (2020), 121361, https://doi.org/10.1016/j.talanta.2020.121361.

[5] W. Gu, H. Zhang, C. Chen, J. Zhang, Study on the design of ZnO/PANI composites and the mechanism of enhanced humidity sensing properties, Curr. Appl. Phys. 34 (2022) 112–121, https://doi.org/10.1016/j.cap.2021.11.013.

[6] D. Wang, D. Zhang, P. Li, Z. Yang, Q. Mi, L. Yu, Electrospinning of flexible Poly (vinyl alcohol)/MXene nanofiber-based humidity sensor self-powered by monolayer molybdenum diselenide piezoelectric nanogenerator, Nano-Micro Lett. 13 (2021) 57, https://doi.org/10.1007/s40820-020-00580-5.

[7] D. Zhang, D. Wang, P. Li, X. Zhou, X. Zong, G. Dong, Facile fabrication of high-performance QCM humidity sensor based on layer-by-layer self-assembled polyaniline/graphene oxide nanocomposite film, Sensors Actuators B Chem. 255 (2018) 1869–1877, https://doi.org/10.1016/j.snb.2017.08.212.

[8] D. Wang, D. Zhang, Y. Yang, Q. Mi, J. Zhang, L. Yu, Multifunctional Latex/Polytetrafluoroethylene-based triboelectric nanogenerator for self-powered organ-like MXene/Metal–Organic framework-derived CuO nanohybrid ammonia sensor, ACS Nano 15 (2021) 2911–2919, https://doi.org/10.1021/acsnano.0c09015.

[9] D. Zhang, Z. Xu, Z. Yang, X. Song, High-performance flexible self-powered tin disulfide nanoflowers/reduced graphene oxide nanohybrid-based humidity sensor driven by triboelectric nanogenerator, Nano Energy 67 (2020), 104251, https://doi.org/10.1016/j.nanoen.2019.104251.

[10] E.E. Ateia, A.T. Mohamed, M. Morsy, Humidity sensor applications based on mesopores LaCoO3, J. Mater. Sci. Mater. Electron. 30 (2019), https://doi.org/10.1007/s10854-019-02284-y.

[11] E.E. Ateia, M.M. Arman, M. Morsy, Synthesis, characterization of NdCoO3 perovskite and its uses as humidity sensor, Appl. Phys. A Mater. Sci. Process. 125 (2019), https://doi.org/10.1007/s00339-019-3168-6.

[12] E.E. Ateia, M.M.A.M. Morsy, Synthesis, characterization of - NdCoO3 perovskite and its uses as humidity sensor, Appl. Phys. A Mater. Sci. Process. (2019) 1–9, https://doi.org/10.1007/s00339-019-3168-6.

[13] H. Parangusan, J. Bhadra, Z. Ahmad, in: ZnO composite electrospun fi bers, RSC Advances, 2021, pp. 28735–28743, https://doi.org/10.1039/d1ra02842a.

[14] H. Parangusan, J. Bhadra, Z. Ahmad, S. Mallick, F. Touati, N. Al-Thani, Capacitive type humidity sensor based on PANI decorated Cu–ZnS porous microspheres, Talanta 219 (2020), 121361, https://doi.org/10.1016/j.talanta.2020.121361.

[15] M.A. Elsayed M. Gobara, Enhancement Removal of Tartrazine Dye Using HCl-doped Polyaniline and TiO2-decorated PANI Particles Enhancement Removal of Tartrazine Dye Using HCl-doped Polyaniline and TiO2-decorated PANI Particles, (n.d.).

[16] C. Li, Electrospun Polyaniline/Poly (ethylene oxide) Composite Nanofibers Based Gas Sensor, University of California, Riverside, 2013. https://www.proquest.com/dissertations-theses/electrospun-polyaniline-poly-ethylene-oxide/docview/1466021988/se-2?accountid=178282.

[17] I. Karbownik, O. Rac-Rumijowska, T. Rybicki, P. Suchorska-Woźniak, H. Teterycz, The effect of temperature on electric conductivity of polyacrylonitrile-polyaniline fibers, IEEE Access. 9 (2021) 74017–74027, https://doi.org/10.1109/ACCESS.2021.3078835.

[18] M. Rahim, A.-U.-H.A. Shah, S. Bilal, I. Rahim, R. Ullah, Highly efficient humidity sensor based on sulfuric acid doped polyaniline-copper oxide composites, iranian journal of science and technology, transactions aScience 45 (2021) 1981–1991, https://doi.org/10.1007/s40995-021-01201-5.

[19] F. Gao, J. Mu, Z. Bi, S. Wang, Z. Li, Recent advances of polyaniline composites in anticorrosive coatings: a review, Prog. Org. Coat. 151 (2021), 106071, https://doi.org/10.1016/j.porgcoat.2020.106071.

[20] A.I. Abdel-Salam, S.Y. Attia, F.I. El-Hosiny, M.A. Sadek, S.G. Mohamed, M. M. Rashad, Facile one-step hydrothermal method for NiCo2S4/rGO nanocomposite synthesis for efficient hybrid supercapacitor electrodes, Mater. Chem. Phys. 277 (2022), 125554, https://doi.org/10.1016/j.matchemphys.2021.125554.
[21] X. Wang H. Wei X. Liu W. Du X. Zhao X. Wang, Novel Three-dimensional Polyaniline Nanothorns Vertically Grown on Buckypaper as High-performance Supercapacitor Electrode, (n.d.).
[22] R. Nashed, E. Girgis, A. Shehata, A.I. Abdel-Salam, M.B. Mohamed, Remarkable enhancement of the photocurrent response of dye-sensitized solar cells using CuInSe2 nanocrystals, in: Asia Communications and Photonics Conference, Optica Publishing Group, Guangzhou, 2012, https://doi.org/10.1364/ACPC.2012.ATh2F.4.
[23] A.I. Abdel-Salam, M.M. Awad, T.S. Soliman, A. Khalid, The effect of graphene on structure and optical properties of CdSe nanoparticles for optoelectronic application, J. Alloys Compd. 898 (2022), 162946, https://doi.org/10.1016/j.jallcom.2021.162946.
[24] T. Ali, M. Shah, Processing and optical characterization of ultra-sensitive humidity and pressure sensors based on polyaniline/holmium oxide hybrid nanocomposites, Sensors Actuators A Phys. 331 (2021), 113040, https://doi.org/10.1016/j.sna.2021.113040.
[25] R.S. Biscaro, M.C. Rezende, R. Faez, Influence of doped polyaniline on the interaction of Pu/PAni blends and on its microwave absorption properties, Polym. Adv. Technol. 19 (2008) 151–158, https://doi.org/10.1002/pat.990.
[26] J. Ma, J. Dai, Y. Duan, J. Zhang, L. Qiang, J. Xue, Fabrication of PANI-TiO2/rGO hybrid composites for enhanced photocatalysis of pollutant removal and hydrogen production, Renew. Energy 156 (2020) 1008–1018, https://doi.org/10.1016/j.renene.2020.04.104.
[27] Y. Chang, J. Lin, S. Wu, One-step growth of Na 2 Ti3O7 nanorods for enhanced photocatalytic activities and recyclability, Journal of Alloys and Compounds. 749 (2018) 955–960, https://doi.org/10.1016/j.jallcom.2018.03.332.
[28] W. Gu, H. Zhang, C. Chen, J. Zhang, Study on the design of ZnO/PANI composites and the mechanism of enhanced humidity sensing properties, Curr. Appl. Phys. 34 (2022) 112–121, https://doi.org/10.1016/j.cap.2021.11.013.
[29] D.A. Kospa, A.I. Ahmed, S.E. Samra, S.A. El-Hakam, A.A. Ibrahim, Flexible CuO-rGO/ PANI thermal absorber with high broadband photoresponse and salt resistance for efficient desalination of oil-contaminated seawater, Desalination 528 (2022), 115612, https://doi.org/10.1016/j.desal.2022.115612.
[30] S. Saad Ali, A. Pauly, J. Brunet, C. Varenne, A.L. Ndiaye, MWCNTs/PMMA/PS composites functionalized PANI: electrical characterization and sensing performance for ammonia detection in a humid environment, Sensors Actuators B Chem. 320 (2020), 128364, https://doi.org/10.1016/j.snb.2020.128364.
[31] P. Singh, S.K. Shukla, Structurally optimized cupric oxide/polyaniline nanocomposites for efficient humidity sensing, Surf. Interfaces. 18 (2020), 100410, https://doi.org/10.1016/j.surfin.2019.100410.
[32] H. Cai, C. Feng, H. Xiao, B. Cheng, Synthesis of Fe3O4/rGO@PANI with three-dimensional flower-like nanostructure and microwave absorption properties, J. Alloys Compd. 893 (2022), 162227, https://doi.org/10.1016/j.jallcom.2021.162227.
[33] Y. Park, A. Numan, N. Ponomarev, J. Iqbal, M. Khalid, Journal of environmental chemical engineering enhanced photocatalytic performance of PANI-rGO-MnO 2 ternary composite for degradation of organic contaminants under visible light, J. Environ. Chem. Eng. 9 (2021), 106006, https://doi.org/10.1016/j.jece.2021.106006.
[34] S. Palsaniya, H.B. Nemade, A. Kumar, Journal of physics and chemistry of solids hierarchical PANI-RGO-ZnO ternary nanocomposites for symmetric tandem supercapacitor, J. Phys. Chem. Solids 154 (2021), 110081, https://doi.org/10.1016/j.jpcs.2021.110081.
[35] S. Kulkarni, P. Patil, A. Mujumdar, J. Naik, Synthesis and evaluation of gas sensing properties of PANI, PANI/SnO2 and PANI/SnO2/rGO nanocomposites at room temperature, Inorg. Chem. Commun. 96 (2018) 90–96, https://doi.org/10.1016/j.inoche.2018.08.008.
[36] J. Ramı, E. Djurado, P. Fabry, in: Synthesis of sodium titanate composites by sol-gel method for use in gas potentiometric sensors 24, 2004, pp. 2477–2483, https://doi.org/10.1016/j.jeurceramsoc.2003.07.014.
[37] T. Ali, M. Shah, Processing and optical characterization of ultra-sensitive humidity and pressure sensors based on polyaniline/holmium oxide hybrid nanocomposites, Sensors Actuators A Phys. 331 (2021), 113040, https://doi.org/10.1016/j.sna.2021.113040.
[38] K. Shan, Z.-Z. Yi, X.-T. Yin, D. Dastan, S. Dadkhah, B.T. Coates, H. Garmestani, Mixed conductivities of A-site deficient Y, Cr-doubly doped SrTiO3 as novel dense diffusion barrier and temperature-independent limiting current oxygen sensors, Adv. Powder Technol. 31 (2020) 4657–4664, https://doi.org/10.1016/j.apt.2020.10.015.
[39] X.-T. Yin, S.-S. Wu, D. Dastan, S. Nie, Y. Liu, Z.-G. Li, Y.-W. Zhou, J. Li, A. Faik, K. Shan, Z. Shi, M.A. Tarighat, X.-G. Ma, Sensing selectivity of SnO2-Mn3O4 nanocomposite sensors for the detection of H2 and CO gases, Surf. Interfaces 25 (2021), 101190, https://doi.org/10.1016/j.surfin.2021.101190.
[40] X.-T. Yin, J. Li, Q. Wang, D. Dastan, Z.-C. Shi, N. Alharbi, H. Garmestani, X.-M. Tan, Y. Liu, X.-G. Ma, Opposite sensing response of heterojunction gas sensors based on SnO2–Cr2O3 nanocomposites to H2 against CO and its selectivity mechanism, Langmuir 37 (2021) 13548–13558, https://doi.org/10.1021/acs.langmuir.1c01706.
[41] W. Zhou, D. Dastan, X. Yin, S. Nie, S. Wu, Q. Wang, J. Li, Optimization of gas sensing properties of n-SnO2/p-xCuO sensors for homogenous gases and the sensing mechanism, J. Mater. Sci. Mater. Electron. 31 (2020) 18412–18426, https://doi.org/10.1007/s10854-020-04387-3.
[42] S. Nie, D. Dastan, J. Li, W.-D. Zhou, S.-S. Wu, Y.-W. Zhou, X.-T. Yin, Gas-sensing selectivity of n-ZnO/p-Co3O4 sensors for homogeneous reducing gas, J. Phys. Chem. Solids 150 (2021), 109864, https://doi.org/10.1016/j.jpcs.2020.109864.
[43] M. Morsy, I.S. Yahia, H.Y. Zahran, F. Meng, M. Ibrahim, in: Portable and Battery Operated Ammonia Gas Sensor Based on CNTs/rGO/ZnO Nanocomposite 48, 2019, pp. 7328–7335, https://doi.org/10.1007/s11664-019-07550-7.
[44] M. Morsy, I.S. Yahia, H.Y. Zahran, M. Ibrahim, Hydrothermal Synthesis of CNTs/Co3O4 @ rGO mesopours Nanocomposite for Enhanced VOCs, Journal of Inorganic and Organometallic Polymers and Materials 29 (2019) 416–422, https://doi.org/10.1007/s10904-018-1011-8.
[45] M. Morsy, M. Helal, M. El-Okr, M. Ibrahim, Preparation and characterization of multiwall carbon nanotubes decorated with zinc oxide, Der Pharma Chem. 7 (2015).
[46] M. Morsy, M.M. Mokhtar, S.H. Ismail, G.G. Mohamed, M. Ibrahim, Humidity sensing behaviour of lyophilized rGO/Fe2O3 nanocomposite, J. Inorg. Organomet. Polym. Mater. 30 (2020) 4180–4190, https://doi.org/10.1007/s10904-020-01570-1.
[47] W.M. Taha, M. Morsy, N.A. Nada, M. Ibrahim, Diamond & Related Materials Studying the humidity sensing behavior of MWCNTs boosted with Co3 O4 nanorods, Diamond Relat. Mater. 121 (2022), 108754, https://doi.org/10.1016/j.diamond.2021.108754.
[48] A. Kumar, S. Banerjee, J.P. Saikia, B.K. Konwar, Swift heavy ion irradiation induced enhancement in the antioxidant activity and biocompatibility of polyaniline nanofibers, Nanotechnology 21 (2010), 175102, https://doi.org/10.1088/0957-4484/21/17/175102.
[49] Z. Wang, J.-J. Han, N. Zhang, D.-D. Sun, T. Han, Synthesis of polyaniline/graphene composite and its application in zinc-rechargeable batteries, J. Solid State Electrochem. 23 (2019) 3373–3382, https://doi.org/10.1007/s10008-019-04435-x.
[50] A.H. Zaki, A.A. Naeim, S.I. EL-Dek, Sodium titanate nanotubes for efficient transesterification of oils into biodiesel, Environmental Science and Pollution Research 26 (2019) 36388–36400, https://doi.org/10.1007/s11356-019-06602-z.
[51] R. Saleh, A.H. Zaki, F.I.A. El-Ela, A.A. Farghali, M. Taha, R. Mahmoud, Consecutive removal of heavy metals and dyes by a fascinating method using titanate nanotubes, J. Environ. Chem. Eng. 9 (2021), 104726, https://doi.org/10.1016/j.jece.2020.104726.
[52] W. Shao, R. Jamal, F. Xu, A. Ubul, T. Abdiryim, The effect of a small amount of water on the structure and electrochemical properties of solid-state synthesized polyaniline, Materials 5 (2012) 1811–1825, https://doi.org/10.3390/ma5101811.
[53] Y. Guo, D. He, S. Xia, X. Xie, X. Gao, Q. Zhang, Preparation of a novel nanocomposite of polyaniline core decorated with anatase-TiO2 nanoparticles in ionic Liquid/Water microemulsion, J. Nanomater. 2012 (2012), 202794, https://doi.org/10.1155/2012/202794.
[54] N. Parveen, M.O. Ansari, M.H. Cho, Route to high surface area, mesoporosity of polyaniline-titanium dioxide nanocomposites via one pot synthesis for energy storage applications, Ind. Eng. Chem. Res. 55 (2016) 116–124, https://doi.org/10.1021/acs.iecr.5b02907.
[55] Y. Zhang, J. Liu, Y. Zhang, Y. Duan, RSC advances facile synthesis of hierarchical nanocomposites of aligned polyaniline nanorods on reduced graphene oxide nanosheets for microwave absorbing, RSC Adv. 7 (2017) 54031–54038, https://doi.org/10.1039/C7RA08794B.
[56] J. Huang, X. Song, C. He, Z. Zhang, L. Qu, D. Zhao, in: Preparation and performance of multiwall carbon nanotubes/FeNi3/polyaniline composite electrode material for supercapacitors, 2020, pp. 2525–2536.
[57] Y. Negr, M. Testa-anta, L. Mar, in: Titanate Nanowires as One-dimensional Hot Spot Generators for Broadband Au – TiO 2 Photocatalysis, 2019, pp. 1–12.
[58] P. Hernández-Hipólito, N. Juárez-Flores, E. Martínez-Klimova, A. Gómez-Cortés, X. Bokhimi, L. Escobar-Alarcón, T.E. Klimova, Novel heterogeneous basic catalysts for biodiesel production: sodium titanate nanotubes doped with potassium, Catal. Today 250 (2015) 187–196, https://doi.org/10.1016/j.cattod.2014.03.025.
[59] T. Jiang, L. Zhang, M. Ji, Q. Wang, Q. Zhao, X. Fu, H. Yin, Particuology carbon nanotubes/TiO2 nanotubes composite photocatalysts for efficient degradation of methyl orange dye, Particuology. 11 (2013) 737–742, https://doi.org/10.1016/j.partic.2012.07.008.
[60] S. Wei, Z. Shi, W. Wei, H. Wang, D. Dastan, M. Huang, J. Shi, S. Chen, Facile preparation of ultralight porous carbon hollow nanoboxes for electromagnetic wave absorption, Ceram. Int. 47 (2021) 28014–28020, https://doi.org/10.1016/j.ceramint.2021.06.132.
[61] E.E. Ateia, M.M. Arman, M. Morsy, Synthesis, characterization of NdCoO3 perovskite and its uses as humidity sensor, Appl. Phys. Mater. Sci. Process. 125 (2019) 1–9, https://doi.org/10.1007/s00339-019-3168-6.
[62] S. Manjunatha, T. Machappa, Y.T. Ravikiran, B. Chethan, A. Sunilkumar, Polyaniline based stable humidity sensor operable at room temperature, Phys. B Condens. Matter 561 (2019) 170–178, https://doi.org/10.1016/j.physb.2019.02.063.
[63] F.-W. Zeng, X.-X. Liu, D. Diamond, K.T. Lau, Humidity sensors based on polyaniline nanofibres, Sensors Actuators B Chem. 143 (2010) 530–534, https://doi.org/10.1016/j.snb.2009.09.050.
[64] M.V. Fuke, A. Vijayan, M. Kulkarni, R. Hawaldar, R.C. Aiyer, Evaluation of co-polyaniline nanocomposite thin films as humidity sensor, Talanta 76 (2008) 1035–1040, https://doi.org/10.1016/j.talanta.2008.04.064.
[65] M.T.S. Chani, K.S. Karimov, F.A. Khalid, S.Z. Abbas, M.B. Bhatty, Orange dye—polyaniline composite based impedance humidity sensors, Chinese Physics B. 22 (2013) 10701, https://doi.org/10.1088/1674-1056/22/1/010701.

[66] S.C. Nagaraju, A.S. Roy, J.B.P. Kumar, K.R. Anilkumar, G. Ramagopal, Humidity sensing properties of surface modified polyaniline metal oxide composites, J. Eng. 2014 (2014), 925020, https://doi.org/10.1155/2014/925020.
[67] S.S. Sandhu, S. Kumar, S. Augustine, U. Saha, K. Arora, S. Bayan, S.K. Ray, N. K. Puri, B.D. Malhotra, Nanoengineered conductive polyaniline enabled sensor for sensitive humidity detection, IEEE Sensors J. 20 (2020) 12574–12581, https://doi.org/10.1109/JSEN.2020.3001599.
[68] Y.-N. Guo, Z.-Y. Gao, X.-X. Wang, L. Sun, X. Yan, S.-Y. Yan, Y.-Z. Long, W.-P. Han, A highly stretchable humidity sensor based on spandex covered yarns and nanostructured polyaniline, RSC Adv. 8 (2018) 1078–1082, https://doi.org/10.1039/C7RA10474J.
[69] S. Kotresh, Y.T. Ravikiran, S.C. Vijaya Kumari, H.G. Raj Prakash, S. Thomas, Polyaniline niobium pentoxide composite as humidity sensor at room temperature, advanced, Mater. Lett. 6 (2015) 641–645, https://doi.org/10.5185/amlett.2015.5795.
[70] H. Parangusan, J. Bhadra, Z. Ahmad, S. Mallick, F. Touati, N. Al-Thani, Humidity sensor based on poly(lactic acid)/PANI–ZnO composite electrospun fibers, RSC Adv. 11 (2021) 28735–28743, https://doi.org/10.1039/D1RA02842A.
[71] K. Shan, F. Zhai, Z.-Z. Yi, X.-T. Yin, D. Dastan, F. Tajabadi, A. Jafari, S. Abbasi, Mixed conductivity and the conduction mechanism of the orthorhombic CaZrO3 based materials, Surf. Interfaces 23 (2021), 100905, https://doi.org/10.1016/j.surfin.2020.100905.
[72] N. Haghnegahdar, M. Abbasi Tarighat, D. Dastan, Curcumin-functionalized nanocomposite AgNPs/SDS/MWCNTs for electrocatalytic simultaneous determination of dopamine, uric acid, and guanine in co-existence of ascorbic acid by glassy carbon electrode, J. Mater. Sci. Mater. Electron. 32 (2021) 5602–5613, https://doi.org/10.1007/s10854-021-05282-1.